kinases and phosphatases

MDPI

*Article*

# Loss of *Tsc2* in Neonatal V-SVZ Neural Stem Cells Causes Rare Malformations

**Jennie C. Holmberg [1,†], Victoria A. Riley [1,†], Aidan M. Sokolov [1], Luke J. Fisher [1] and David M. Feliciano [1,2,*]**

[1] Department of Biological Sciences, Clemson University, Clemson, SC 29631, USA
[2] Center for Human Genetics, Clemson University, Greenwood, SC 29646, USA
* Correspondence: dfelici@clemson.edu; Tel.: +1-864-656-2328; Fax: +1-864-656-0435
† These authors contributed equally to this work.

**Abstract**

Tuberous Sclerosis Complex (TSC) is a genetic disorder caused by mutations that inactivate *TSC1* or *TSC2* genes. *TSC1* or *TSC2* mutations activate the mammalian target of rapamycin complex 1 (mTORC1) protein kinase pathway. Although many patients inherit a single copy of a mutant *TSC* gene, somatic mutations that cause loss of heterozygosity in inhibitory neuroprogenitor cells are hypothesized to be one cause of abnormal development. This may lead to cortical malformations or benign growths along the ventricular-subventricular zone (V-SVZ), cortex, olfactory tract, and olfactory bulbs (OB). This idea is supported by focal single-cell knockout experiments that induce CRE-mediated recombination following neonatal electroporation of conditional *Tsc2* or *Tsc1* mice. Loss of *Tsc2* causes mTORC1 pathway activation and the formation of striatal hamartomas composed of ectopic clusters of abnormal cells and cytomegalic neurons, including within the OB. Neural phenotypes in this model can be partially rescued with Rapalink-1, a bisteric mTOR inhibitor, demonstrating the importance of mTOR in pathogenesis. We previously demonstrated that global V-SVZ neural stem cell (NSC) *Tsc2* mutation induced by *nestin*-CRE-ER$^{T2}$ causes mTORC1 pathway activation, which is accompanied by transcriptional and translational errors. While we previously described cultured NSCs and OB granule cells from these mice, we did not thoroughly describe changes outside this region. Here, we provide evidence that removal of *Tsc2* from neonatal V-SVZ NSCs causes subtle and rare brain malformations. This is exemplified by ectopic clusters of cytomegalic neurons and mTORC1 activation. This data supports that loss of *Tsc2* in NSCs during neonatal development leads to heterotopic clusters in the adult brain. This model may be useful to study TSC, but the rarity and stochastic nature of lesions make the use challenging for identifying mechanisms and testing therapies.

**Keywords:** *Tsc2*; *Tsc1*; Tuberin; Tuberous Sclerosis Complex; TSC; mTOR

Check for updates

Academic Editor: Mauro Salvi

Received: 14 December 2025
Revised: 24 February 2026
Accepted: 26 February 2026
Published: 3 March 2026

**Copyright:** © 2026 by the authors. Licensee MDPI, Basel, Switzerland. This article is an open access article distributed under the terms and conditions of the Creative Commons Attribution (CC BY) license.

## 1. Introduction

Tuberous Sclerosis Complex (TSC) is a disease that affects several tissue types, including the nervous system, and cell types, including neurons [1–3]. The underlying cause of TSC is inactivating mutations in the *TSC1* or *TSC2* genes found on chromosomes 9q34 and 16p13.3, respectively [4,5]. These mutations most often cause the loss of expression of the proteins encoded by *TSC1/TSC2* through nonsense and missense mutations, deletions, and large rearrangements [6]. Loss of function of *TSC1/TSC2* causes unrestrained mTORC1 activity [2]. TSC is considered an autosomal dominant disorder [6]. Patients who are afflicted

with TSC are frequently born with congenital malformations or develop growths called hamartomas [1,7]. Brain malformations are associated with a wide range of neurological manifestations [1].

TSC is proposed to follow Alfred Knudson's two-hit hypothesis, wherein pathogenic mutations in one copy of the TSC genes may occur early in development or be inherited [8,9]. However, "second-hit" mutations occur in the other normal (wild-type) copy of this gene. Knudson used the Eker rat, which has a germ-line transmissible *Tsc2* variant caused by a transposon-like insertion of an inactive 6253 base pair intracisternal A-particle element containing multiple termination codons to demonstrate TSC growths adhere to the two-hit hypothesis [10,11]. This insertion is 3′ to the catalytic domain of the encoded protein Tuberin. Eker rats homozygous for this mutation fail to develop. However, 30–60% of heterozygous Eker rats develop CNS malformations that are reminiscent of those seen in patients [12,13]. The prevalence and severity of brain hamartomas increases when Eker rats are exposed to radiation or mutagens [13]. Loss of heterozygosity (LOH) and mTORC1 activation occur in these hamartomas [14–16]. These results support the two-hit hypothesis as a mechanism that is sufficient to cause TSC malformations [15,16]. Forty-three heterozygous Eker rats subject to necropsy demonstrated that 100% have renal tumors, 48% have subependymal hamartomas, 21% have subcortical hamartomas, 33% have meningiomas, and 58% have pituitary adenomas [12]. These results demonstrate that the *Tsc2* gene is critically required in numerous cell types of different brain regions, consistent with the vast heterogeneity of lesions found in patients, and support an evolutionarily conserved role of TSC genes. Hamartomas often arise within the striatum near the caudate nucleus, reminiscent of subependymal nodules (SENs) or subependymal giant cell astrocytomas (SEGAs). More recently, the Eker rat has been revisited with demonstration of loss of neurons in the caudate, microglia activation, vasculature remodeling, gliosis, and increased neural stem cell (NSC) marker expression [17].

Given the location and timing of SEN/SEGA appearance, it has been hypothesized that LOH mutations in NSCs along the ventricular–subventricular zone (V-SVZ) might be the cause. Indeed, several mouse models have explored this possibility with significant overlap in agreement with the appearance of SEGAs in the Eker model [18–22]. In one of these models, loss of *Tsc1* resulted in nodules along the lateral ventricles and large growths at the base of the lateral ventricles [18]. This could be achieved by removing *Tsc1* from Nestin-expressing NSCs or transit amplifying cells, an intermediate progenitor of the V-SVZ. These growths were accompanied by fewer olfactory bulb (OB) granule cells. Similar abnormalities, including heterotopic clusters of cytomegalic neurons, were produced by CRE electroporation and/or using *Tsc1* × *Nestin*-CRE-ER$^{T2}$ mice [19]. In another study, *Tsc1* and *PTEN* were removed at P10 or P15–17 using *Nestin*-CRE-ER$^{T2}$ [20]. Mice developed SEN-like and SEGA-like growths in ~1 month and shared overlapping histopathological features with patient SENs and SEGAs.

Loss of *TSC2* is, however, the most common genetic cause of SEGAs. Neonatal electroporation of conditional *Tsc2* mice with CRE recombinase caused the formation of both intraventricular anomalies and hamartomas within the boundaries of the V-SVZ and striatum [21]. Fluorescent activated nuclei sorting (FANS) and single nuclei RNA sequencing demonstrated changes in NSC transitional states accompanied by the differential expression of stem and progenitor transcripts [21,23]. In vivo, neonatal lateral V-SVZ NSCs have high mTORC1 activity but generate striatal glia with low mTORC1 activity. Loss of *Tsc2* prevented glia from downregulating mTORC1 activity. As expected, aberrant translation of NSC proteins occurred. The striatal hamartomas can be partially rescued with Rapalink-1, a bisteric mTOR inhibitor, demonstrating the importance of mTOR in pathogenesis [24].

We also crossed *Nestin*-CRE-ER$^{T2}$ mice to conditional *Tsc2* mice and cultured mutant NSCs [21]. Cultured NSCs had altered transcriptomes with differences in many ribosomal RNAs and translational regulatory RNAs. Predictably, NSC mRNA translational programs are also altered in vitro. We further reported that OB granule cells from these mice have elevated mTORC1 activity and that the average soma size is enlarged [25]. These changes were corroborated by the neonatal electroporation model. However, the V-SVZs from these same *Nestin*-CRE-ER$^{T2}$ mice were not reported. Here, we provide corroborating evidence that loss of *Tsc2* from V-SVZ NSCs using *Nestin*-CRE-ER$^{T2}$ mice causes brain pathology consistent with TSC patients, notably increased mTORC1 activity and ectopic clusters of cytomegalic cells.

## 2. Results

### *2.1. Targeted Recombination in Gliogenic and Neurogenic Stem Cells*

The *Nestin* gene promoter drives selective expression of the intermediate filament structural protein, Nestin, in NSCs. Knockin mice have been engineered to contain the rat *Nestin* promoter downstream of sequences encoding a Cre recombinase fused to a modified estrogen receptor (ER$^{T2}$), which can be used to manipulate NSCs and their progeny [26]. Application of (4-OH) tamoxifen causes the modified ER$^{T2}$ to dimerize in the cytoplasm and transiently translocate CRE into the nuclear compartment, where it subsequently excises DNA flanked by *loxP* sites. These *Nestin*-CRE-ER$^{T2}$ mice were mated to mice having wild-type or conditional *Tsc2* alleles (*Tsc2*$^{tm1.1Mjg}$/J) containing *loxP* sites flanking exons 2,3, and 4 (henceforth referred to as *Tsc2*$^{f/f}$). These mice were also crossed to Ai9 mice (B6.Cg-*Gt(ROSA)26Sor*$^{tm9(CAG-tdTomato)Hze}$/J) that have a *loxP*-flanked STOP cassette that prevents transcription of a CAG-promoter driven variant of red fluorescent protein (tdTomato, RFP). CRE-ER$^{T2}$ will therefore remove the stop sequence and induce RFP expression and *Tsc2* recombination, thereby generating mutant *Tsc2*$^{mut/mut}$ cells, including those where NSCs are located, along the lateral ventricle (Figure 1A) [26].

We previously demonstrated that neonatal application of tamoxifen induced robust *Tsc2* recombination in the V-SVZ, where NSCs exist [21,25]. V-SVZ NSCs cultured from these mice also had detectable *Tsc2* genomic recombination and loss of the encoded protein Tuberin. V-SVZ NSCs generate OB granule cells in vivo. Indeed, rapid and sustained *Tsc2* recombination could be detected in OB granule cells. We demonstrated recombination of the *Tsc2* gene as early as P10 but did not examine the developmental consequences in these previously published manuscripts. We confirmed recombination as indicated by robust RFP expression in DCX-positive neuroblasts entering the olfactory bulb (Figure 1B,C). However, recombination in NeuN-positive OB granule cells was sparse at this age (Figure 1B,C). RFP and NeuN double-positive cells were absent from the striatum and cortex as well (Figure 1D,E). There was robust labeling of cells having a glial/astrocyte morphology in the striatum and cortex (Figure 1D,E). RMS neuroblasts and striatal and cortical astrocytes are produced from V-SVZ NSCs. Tuberin staining was reduced in *Tsc2*$^{mut/mut}$ RFP positive cells (Figure 1F–I). Robust RFP expression was confirmed in V-SVZ NSCs, both based on the location and morphology of cells and their high Vimentin expression, Sox2 expression, and proliferation indicated by incorporation of the thymidine analog EdU injected immediately prior to sacrifice (Figure 1J–Q). RFP and DCX double-positive neuroblasts formed migratory chains strewn among RFP positive NSCs labeled with Vimentin or Nestin (Figure 1N–Q). These results confirm the selective targeting of gliogenic and neurogenic stem cells.

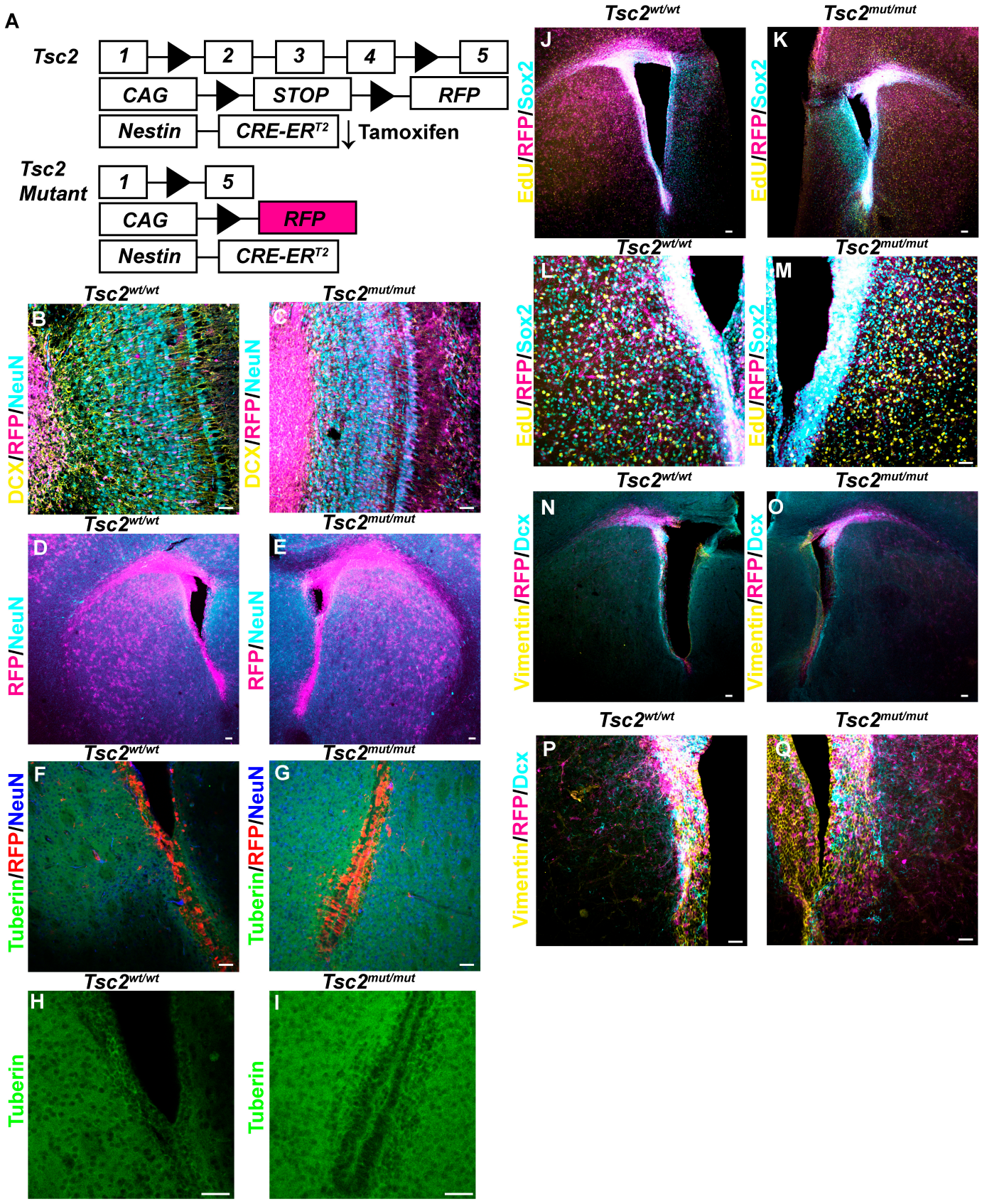



**Figure 1.** Targeted Recombination in Gliogenic and Neurogenic Stem Cells (**A**). Schematic diagram of conditional *Tsc2* deletion. (**B**,**C**). 20× image of coronal section of an olfactory bulb from *Tsc2*$^{wt/wt}$ (**B**) or *Tsc2*$^{mut/mut}$ (**C**), demonstrating that most RFP positive cells (magenta) are neuroblasts and are DCX-positive (yellow), not NeuN-positive (cyan). (**D**,**E**). 5× image of coronal section of *Tsc2*$^{wt/wt}$ (**D**) or

*Tsc2*$^{mut/mut}$ (**E**) at P10 demonstrating RFP positive cells (magenta) along the lateral ventricle and Neu-N (cyan) to mark neurons. (**F**,**G**). 20× image of coronal section from *Tsc2*$^{wt/wt}$ (**F**) or *Tsc2*$^{mut/mut}$ (**G**) at P10 demonstrating RFP positive cells (red) along the lateral ventricle, Tuberin (green), and NeuN, which labels neurons (blue) in *Tsc2*$^{wt/wt}$ (**F**) or *Tsc2*$^{mut/mut}$ (**G**). (**H**,**I**). 20× zoom-2 image of (**F**,**G**) demonstrating loss of Tuberin from *Tsc2*$^{mut/mut}$ cells. (**J**,**K**). 5× image of coronal section from *Tsc2*$^{wt/wt}$ (**J**) or *Tsc2*$^{mut/mut}$ (**K**) at P10 demonstrating that RFP positive cells (magenta), EdU (yellow), and Sox2 positive neuroprogenitors (cyan). (**L**,**M**). 20× images of (**J**,**K**). (**N**,**O**). 5× image of coronal section from *Tsc2*$^{wt/wt}$ (**N**) or *Tsc2*$^{mut/mut}$ (**O**) at P10 demonstrating that RFP positive cells (magenta), DCX positive neuroblasts (cyan), and Vimentin positive neuroprogenitors (yellow). (**P**,**Q**). 20× images of (**N**) and (**O**). Scale bar = 50 μm.

### *2.2. Loss of Tsc2 in NSCs Increases mTORC1 Activity*

We confirmed that at this early age (P10), V-SVZ cells, including NSCs expressing Nestin, had low but detectable mTORC1 activity as indicated by phosphorylated (p) 4EBP (Thr37/46) staining (Figure 2A–C). Loss of *Tsc2* caused minor changes in mTORC1 activation at P10 (Figure 2D–F). However, *Tsc2* mutant V-SVZs had elevated p4EBP levels by P30 (Figure 2G–N). This result was most notable within the ventral V-SVZ (Figure 2I,J,M,N). RFP positive cells with an astrocyte morphology had little p4EBP in wild-type cells. Incidentally, blood vessels and occasional cells outside of the V-SVZ were strongly p4EBP positive. Remarkably, in some sections, *Tsc2* mutant cells failed to down-regulate mTORC1 as they invaded the striatum and retained high p4EBP (Figure 2O,P). We quantified p4EBP levels and found a ~32% increase in V-SVZ *Tsc2* mutant cells (*Tsc2*$^{wt/wt}$ = 3.085 ± 0.2469, N = 5 vs. *Tsc2*$^{mut/mut}$ = 4.084 ± 0.2354, N = 5, $p = 0.0190$) (Figure 2Q). We also noted a ~61% expansion of the V-SVZ (*Tsc2*$^{wt/wt}$ = 21,152 ± 2576, N = 5 vs. *Tsc2*$^{mut/mut}$ = 33,998 ± 4657, N = 5, $p = 0.0423$) (Figure 2R). Furthermore, loss of *Tsc2* increased mTORC1 in striatal glia (*Tsc2*$^{wt/wt}$ = 22.39 ± 0.9998, n = 201 vs. *Tsc2*$^{mut/mut}$ = 30.78 ± 1.503, n = 180, $p < 0.0001$) (Figure 2S). These results support that mTORC1 is active in the V-SVZ in stem/progenitor cells and that mTORC1 typically decreases during striatal gliogenesis, but removal of *Tsc2* prevents this from happening.

### *2.3. Cellular Phenotypes Associated with Tsc2 Mutation*

One of the fundamental questions that we entertained was whether abnormal cells might be produced in this model, similar to electroporation models and *Nestin*-CRE-ER$^{T2}$ × *Tsc1* models. We first sought to confirm the cell types and regions labeled. P30 neurogenic regions, including the lateral ventricles and hippocampus, were thoroughly labeled by RFP as seen in sagittal sections (Figure 3A–D). The dentate gyrus of the hippocampus contains Nestin-expressing cells that produce neurons that are NeuN positive. We confirmed the neurogenic potential of these cells and identified NeuN-positive granule cells having excitatory neuron morphologies, which had axons that project along mossy fiber tracts to CA3 (Figure 3A,B,E). Cells along the ventricle included Nestin and GFAP-positive NSCs (Figure 3F–H). NSCs generated striatal cells, including glutamine synthetase-positive striatal glia having an astrocyte morphology (Figure 3I,J). We also found cells having a giant cell-like morphology that were glutamine synthetase negative (Figure 3I,J). We found that Sox2 was detectable at low levels in astrocytes; however, occasional cells having an ambiguous giant cell morphology with large ovoid Sox2-positive nuclei were present in the striatum of all mutant mice examined (Figure 3K,L). The large cells having a neuron-like soma lacked glutamine synthetase but expressed the neuron marker, NeuN (Figure 3M,N). These large cells were found at both the dorsal and, more frequently, the ventral portions of the V-SVZ. We overcame potential concerns that hyperexcitability might cause non-cell autonomous changes leading to ectopic Sox2 expression by analyzing striatal *Tsc2*$^{mut/mut}$ cells from CRE electroporated mice. Sox2 levels were elevated in *Tsc2*

mutant striatal glia compared to *Tsc2* wild-type striatal glia ($Tsc2^{wt/wt}$ = 1.000 ± 0.03584, n = 45 vs. $Tsc2^{mut/mut}$ = 1.150 ± 0.03730, n = 105, $p < 0.05$) (Figure 3O). These results confirm the cell types generated from V-SVZ NSCs, which include glia and giant-like cells that express Sox2 and NeuN.

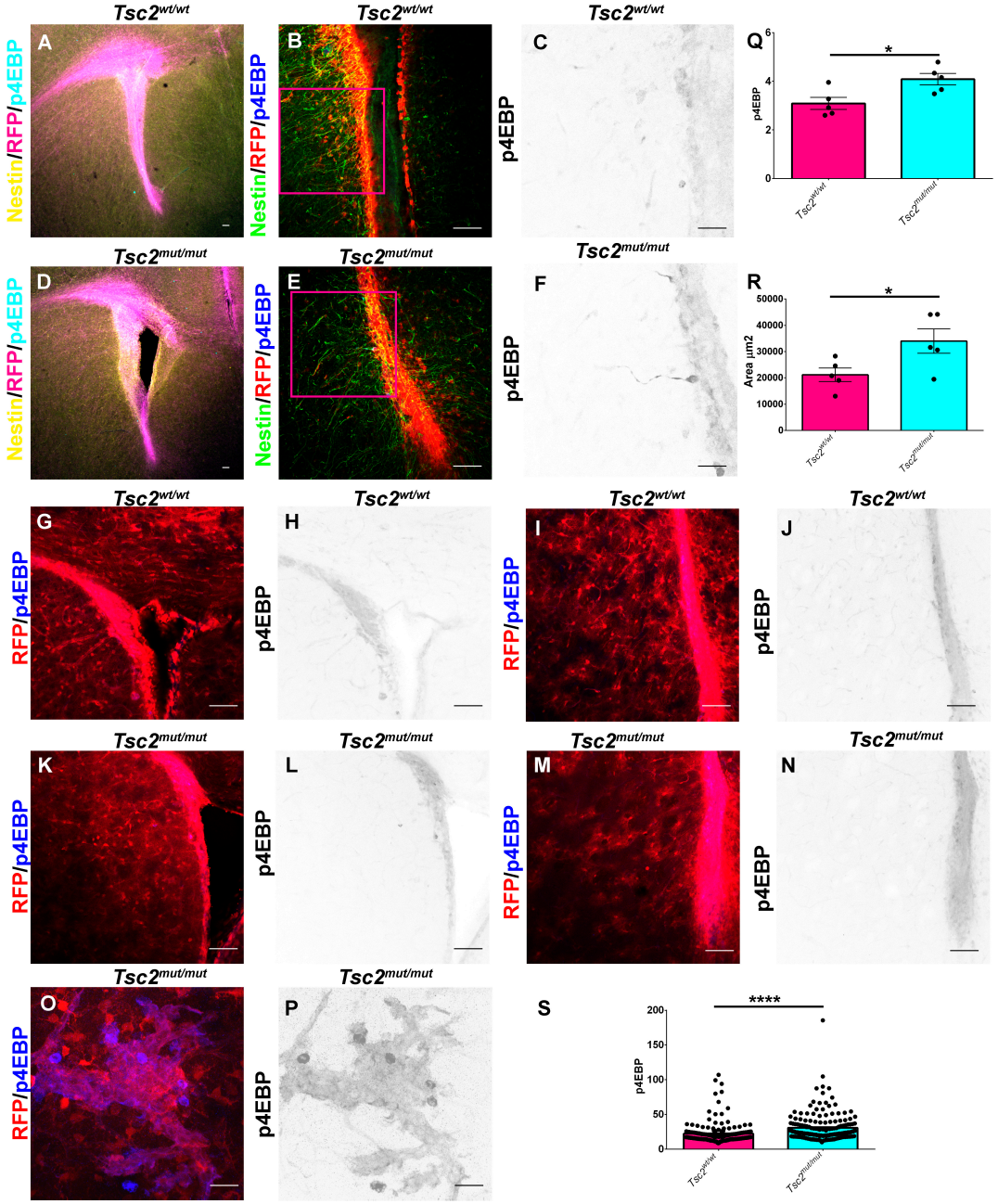



**Figure 2.** Loss of *Tsc2* in NSCs Increases mTORC1 Activity. (**A**) 5× image of coronal section of a P10 $Tsc2^{wt/wt}$ demonstrating RFP (magenta) in Nestin (yellow) positive cells in the V-SVZ and stained for p4EBP (cyan). (**B**,**C**) 20× (**B**) and 40× digital zoom (**C**) demonstrating that p4EBP (blue) staining is mostly along the V-SVZ, where RFP (red) Nestin-positive NSCs (green) are located. The pink box in (**B**) is the region magnified in (**C**). (**D**) 5× image of coronal section of a P10 $Tsc2^{mut/mut}$ demonstrating RFP (magenta) in Nestin (yellow) positive cells in the V-SVZ and stained for p4EBP (cyan). (**E**,**F**). 20× (**E**) and 40× (**F**) digital zoom demonstrating that p4EBP (black) staining is mostly in the V-SVZ, where RFP (red) Nestin (green) positive NSCs are located, and in an outer V-SVZ NSC. The pink box in (**E**) is the region magnified in (**F**). (**G**–**J**) 20× images of coronal sections of a P30 $Tsc2^{wt/wt}$ in the upper (**G**,**H**) or lower V-SVZ (**I**,**J**) showing RFP (magenta) and p4EBP (blue). (**K**–**N**) 20× images of coronal sections of a P30 $Tsc2^{mut/mut}$ in the upper (**K**,**L**) or lower V-SVZ (**M**,**N**) showing RFP (magenta) and

p4EBP (blue). (**O**,**P**) 63× image of coronal section with up-regulated p4EBP within the striatum of heterotopically placed cells. (**Q**) Quantification of p4EBP in the V-SVZ of $Tsc2^{wt/wt}$ and $Tsc2^{mut/mut}$ NSCs. (**R**) Quantification of V-SVZ area. (**S**) Quantification of p4EBP in striatal glia. Scale bar (**A**,**B**,**D**,**E**,**G**–**N**) = 50 µm. Scale bar = 100 µm for (**C**,**F**). Scale Bar = 157.5 µm (**O**,**P**). * = $p < 0.05$, **** = $p < 0.0001$.

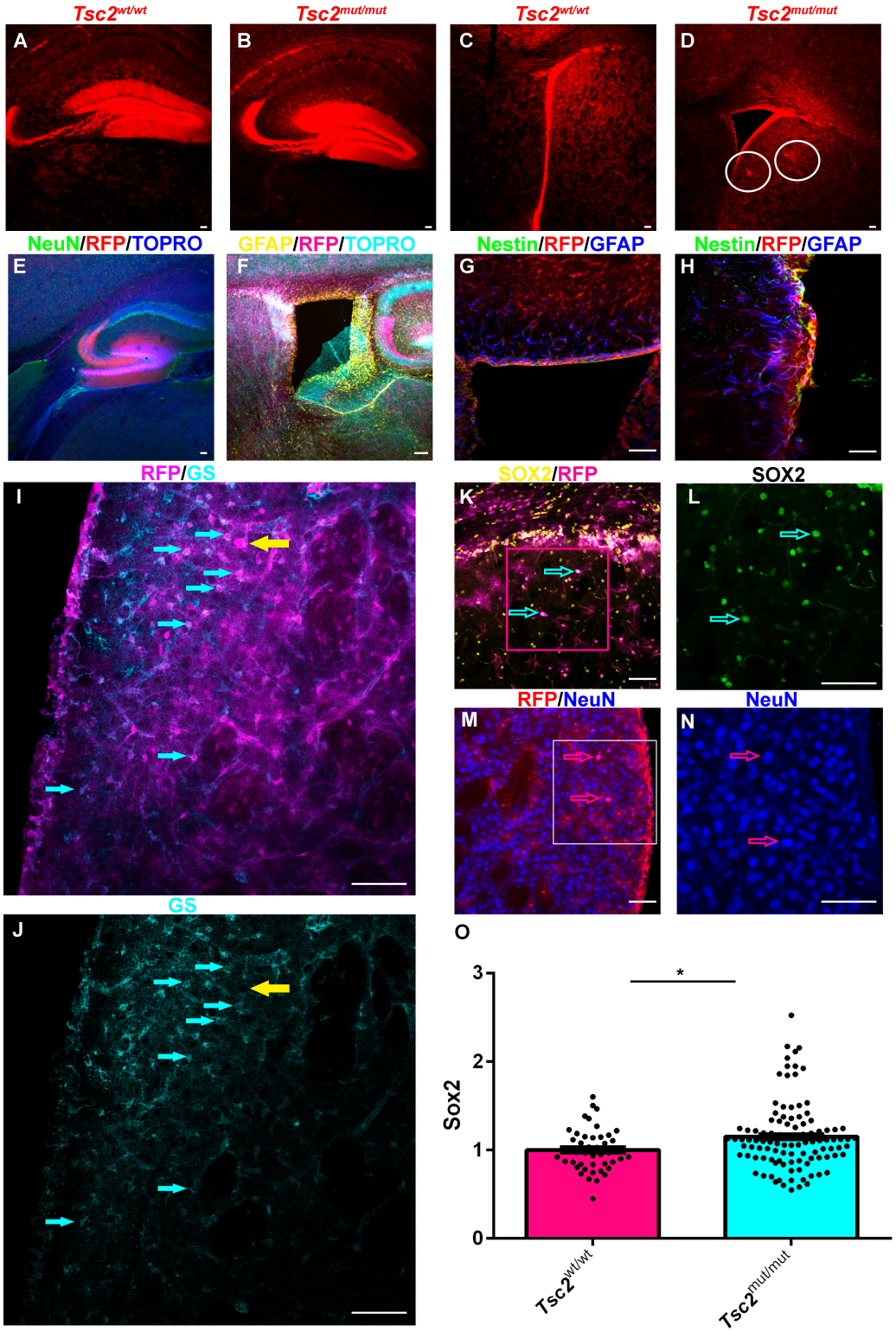



**Figure 3.** Cellular Phenotypes Associated with *Tsc2* Mutation. (**A**,**B**) 5× image of a coronal section of a P30 $Tsc2^{wt/wt}$ (**A**) or $Tsc2^{mut/mut}$ (**B**) brain demonstrating RFP (red) labeling of the hippocampus. (**C**,**D**) 5× image of a coronal section of a P30 $Tsc2^{wt/wt}$ (**C**) or $Tsc2^{mut/mut}$ (**D**) brain demonstrating RFP (red) labeling of the V-SVZ. Circles in (**D**) denote the presence of abnormal organization of the striatum.

(**E**) 5× image of a sagittal section of a P30 *Tsc2*$^{mut/mut}$ brain with RFP (magenta) positive hippocampus, NeuN (green), and the DNA counterstain TO-PRO-3 (blue) showing labeling of neurons in the dentate gyrus of the hippocampus. (**F**–**H**) 10× (**F**), or 20× (**G**,**H**) image of a sagittal section of a P30 *Tsc2*$^{mut/mut}$ brain with RFP (red) positive cells surrounding the ventricle with the NSC marker Nestin (green), and GFAP (**F**) (yellow) (**G**,**H**) (blue), which labels both NSCs and astrocytes. (**I**,**J**) 20× image of a coronal section of a P30 *Tsc2*$^{mut/mut}$ brain with RFP (magenta) and cells having a glial morphology, which stain positive for glutamine synthetase (cyan), denoted by cyan arrows, or a giant cell that is glutamine synthetase negative and denoted by a yellow arrow. (**K**,**L**) 20× image of a coronal section of a *Tsc2*$^{mut/mut}$ brain showing cytomegalic Sox2-positive (yellow) cells in the striatum, indicated by cyan arrows. The magenta box was magnified 2× digitally (**L**), and only Sox2 is shown (green) with cyan arrows highlighting the enlarged nucleus of the cytomegalic cells. (**M**,**N**) 20× image of the lateral portion of a coronal section of a P30 *Tsc2*$^{mut/mut}$ brain with RFP (red), and NeuN (blue) in two cytomegalic neurons. The white box was magnified 2× digitally (**N**) and only NeuN is shown (blue) with magenta arrows highlighting the enlarged nuclei of the cytomegalic cells. (**O**) Quantification of Sox2 levels in RFP positive striatal cells. Scale bar (**A**,**B**,**D**,**E**,**G**–**N**) = 50 µm. * = $p < 0.05$.

### *2.4. Loss of Tsc2 Models TSC Brain Pathological Features*

Brains exhibited pathological hallmarks of TSC by P30. We calculated the penetrance as the percentage of tamoxifen-injected *Nestin*-CRE-ER$^{T2}$ × *Tsc2*$^{f/f}$ × RFP mice that had heterotopic clusters of cells that were independently verified by two scientists. This measurement was chosen since TSC patients have distinct regions of ectopic cells, hamartomas, and dysplasias. 54.5% of mice at P30 (6/11) had heterotopic clusters whereas no *Tsc2*$^{wt/wt}$ mice had heterotopic clusters. 71.4% of tamoxifen injected *Nestin*-CRE-ER$^{T2}$ × *Tsc2*$^{f/f}$ × RFP mice had heterotopic clusters at P60. These results are similar to those reported for Eker rats. However, the expressivity of heterotopic clusters varied. For example, we previously reported multinucleated giant cells in the cortex from these *Tsc2*$^{mut/mut}$ mice [21]. These cortical malformations had fewer neurons around giant/balloon cells (Figure 4A–D). The giant cells were pS6 (240/244) positive (Figure 4E,F). In some cases, especially in the sagittal sections, the caudate nucleus of the striatum appeared to protrude into the ventricle (Figure 4G,H). In many coronal brain sections this was not apparent (Figure 4I–L) and appeared as mostly astrocytes within the striatum. In those sections containing striatal abnormalities, they included disorganization with neurons strewn around the lateral and ventral striatum or clustered non-neuronal cells having an indistinct morphology (Figure 4M–P).

### *2.5. Astrocytes Are Altered in TSC*

NSC mTORC1 activity is tightly regulated during cortical development and along the V-SVZ [22]. NSC mTORC1 activity is high in active NSCs and progenitors called transit amplifying cells (TACs) [27–29]. mTORC1 activity is transiently reduced in early neuroblasts and is very low in astrocytes. mTORC1 activity is required for NSCs and progenitors to transition to an active state. Expression of constitutively active Rheb in these populations increases intermediate progenitors (TACs) along the dorsolateral portion of the V-SVZ [28]. Yet removing *Tsc* genes does not cause unrestricted proliferation. For example, loss of *Tsc2* in lateral V-SVZ NSCs alters transcription and increases select translation factors [21]. Mutant *Tsc2* V-SVZ NSCs alter translation of critical neurodevelopmental mRNAs. In many cases, V-SVZ *Tsc2* null NSCs generate striatal astrocytes that aberrantly translate NSC transcripts, leading to hamartoma-like lesions [21].

Loss of *Tsc* genes from embryonic dorsal radial glia alters cortical development [30–32]. Radial glia affecting cortical layer II/III pyramidal neurons are especially sensitive to loss of *TSC* genes, leading to lamination defects. Indeed, a recent report demonstrated that loss of Tsc1/Tsc2 increases the number of Tbr2-positive intermediate progenitors, thereby expanding upper-layer neurogenesis, layer II/III cortical neurons, and causing macrocephaly [33]. However, excessive mTORC1 activity can also reduce NSC proliferation and cause microcephaly [34]. Cortical astrocytes are also produced from dorsal radial glia. We wondered whether loss of *Tsc2* from Nestin-expressing cells during the neonatal period would affect cortical gliogenesis too. RFP positive cells were nearly evenly distributed in $Tsc2^{wt/wt}$ brains except for the V-SVZ and corpus callosum due to the presence of NSCs and oligodendrocytes, respectively (Figure 5A). Although the gross anatomy of $Tsc2^{mut/mut}$ brains appeared similar, the distribution of glia appeared altered (Figure 5B). The glial identity of cells was confirmed by glutamine synthetase staining (Figure 3I. The region measuring from the ventricle to the pia surface was smaller than $Tsc2^{wt/wt}$ brains ($Tsc2^{wt/wt}$ = 959.7 ± 24.20, N = 6 vs. $Tsc2^{mut/mut}$ = 885.9 ± 20.12, N = 6, $p$ = 0.0410) (Figure 5C). This minor (8%) size and marginally significant measurement at first appearance seems to be unlikely relevant. However, it was accompanied by an RFP barren lower cortical layer that had remarkably fewer glia ($Tsc2^{wt/wt}$, N = 6 vs. $Tsc2^{mut/mut}$, N = 6) (Figure 5D). This was accompanied by ~33% reduction in $Tsc2^{mut/mut}$ RFP cells ($Tsc2^{wt/wt}$, 38,178 ± 1742, N = 6 vs. $Tsc2^{mut/mut}$, 25,421 ± 2917, N = 6, $p$ = 0.0038). To provide additional mechanistic insight into the extent to which astrocytes might be changed in TSC, we examined the differentially expressed transcripts of $Tsc2^{wt/wt}$ or $Tsc2^{mut/mu}$ astrocytes from our recently reported mouse snRNA-sequencing dataset or from our TSC patient SEGAs snRNA-sequencing dataset [21,35]. Like cultured V-SVZ NSCs, the GO term translation was the most significantly enriched term for differentially expressed transcripts in $Tsc2^{mut/mut}$ astrocytes (Figure 5E). Additional alterations included changes to the glutamate receptor signaling pathway, neuronal system, response to copper ion, response to metal ion, and regulation of axon development. Protein–protein Interaction Enrichment Analysis identified changes to many translation and cytoplasmic ribosomal proteins and included the Ribosome-associated Quality Trigger Complex that dissociates a ribosome stalled on a no-go mRNA (Figure 5F,G). These included proteins such as RPL26 (Figure 5H,I), which we previously demonstrated was changed in $Tsc2^{mut/mut}$ NSCs cultured from *Nestin*-CRE-ER$^{T2}$ mice and analyzed by Western blot in V-SVZ cell cultures. We further confirmed the modulation of numerous GO term-enriched RNAs in TSC patient SEGA astroyctes including chemical synaptic transmission, neuron projection development, regulation of synapse organization, brain development, and monoatomic cation transmembrane transport (Figure 5J–L). Encoded proteins regulate synaptic signaling, cell–cell adhesion, behavior, and brain development (Figure 5M,N). Many differentially expressed transcripts overlap with those found in cells from the caudate nucleus (Figure 5M). This agrees with the previous hypothesis that SEGAs may represent abnormal groups of cells from the caudate nucleus. Cell type signature analysis of differentially expressed astrocyte transcripts indicated that the patient transcripts are enriched in those found in midbrain neurotypes, including radial glia-like cells and cortical astrocytes (Figure 5N). These were predicted to be regulated by transcription factors previously implicated in TSC, including NFKB1, RELA, SP1, JUN, STAT, EGR1, and HIF1A, among others. (Figure 5O). Altogether, these results confirm changes to astrocytes in TSC.

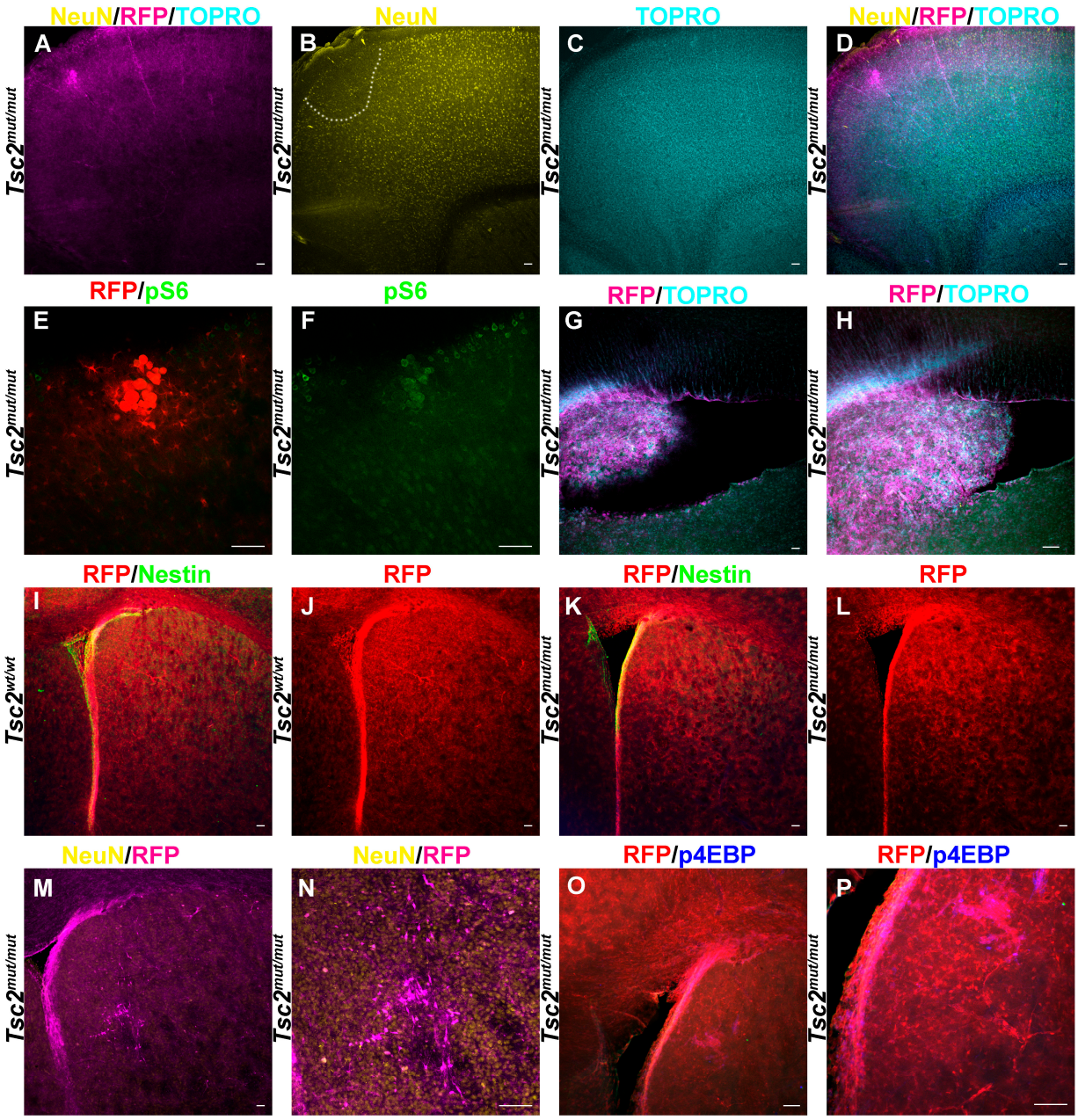



**Figure 4.** Loss of *Tsc2* Models TSC Brain Pathological Features. (**A**–**D**) 5× image of coronal section of a P30 $Tsc2^{mut/mut}$ demonstrating RFP (magenta) (**A**) positive cells forming a lesion in the cerebral cortex. The lesion had sparse neurons, indicated by NeuN staining (yellow) (**B**). Although the cortex did not generally appear mislaminated as seen with the counterstain TO-PRO-3 (cyan) (**C**), which labels DNA, unless the composite (**D**) is examined. (**E**,**F**) 20× image of the lesion in (**A**–**D**) demonstrating that RFP positive (red) (**E**) giant/balloon cells are also pS6-positive (green) (**F**). (**G**) 5× or (**H**) 20× image of a sagittal section of a P30 $Tsc2^{mut/mut}$ demonstrating RFP (red) positive cells protruding into the lateral ventricles. (**I**) 5× image of a coronal section of a P30 $Tsc2^{wt/wt}$ brain demonstrating RFP (red) positive cells together with Nestin staining (green) around the ventricle, or RFP alone (**J**) to show organization of the striatum. (**K**) 5× image of a coronal section of a P30 $Tsc2^{mut/mut}$ brain demonstrating RFP (red) positive cells together with Nestin staining (green) or RFP alone (**L**) to show organization of a typical brain without a lesion. (**M**) 5× or 20× (**N**) image of a coronal section of a P30 $Tsc2^{mut/mut}$ brain demonstrating RFP (magenta) and NeuN staining (yellow) positive cells and a striatal lesion made of disorganized neurons. (**O**) 5× or 20× (**P**) image of a coronal section of a P30 $Tsc2^{mut/mut}$ brain demonstrating RFP (magenta) and p4EBP staining (blue) positive cells and a striatal lesion made of disorganized glia-like cells.

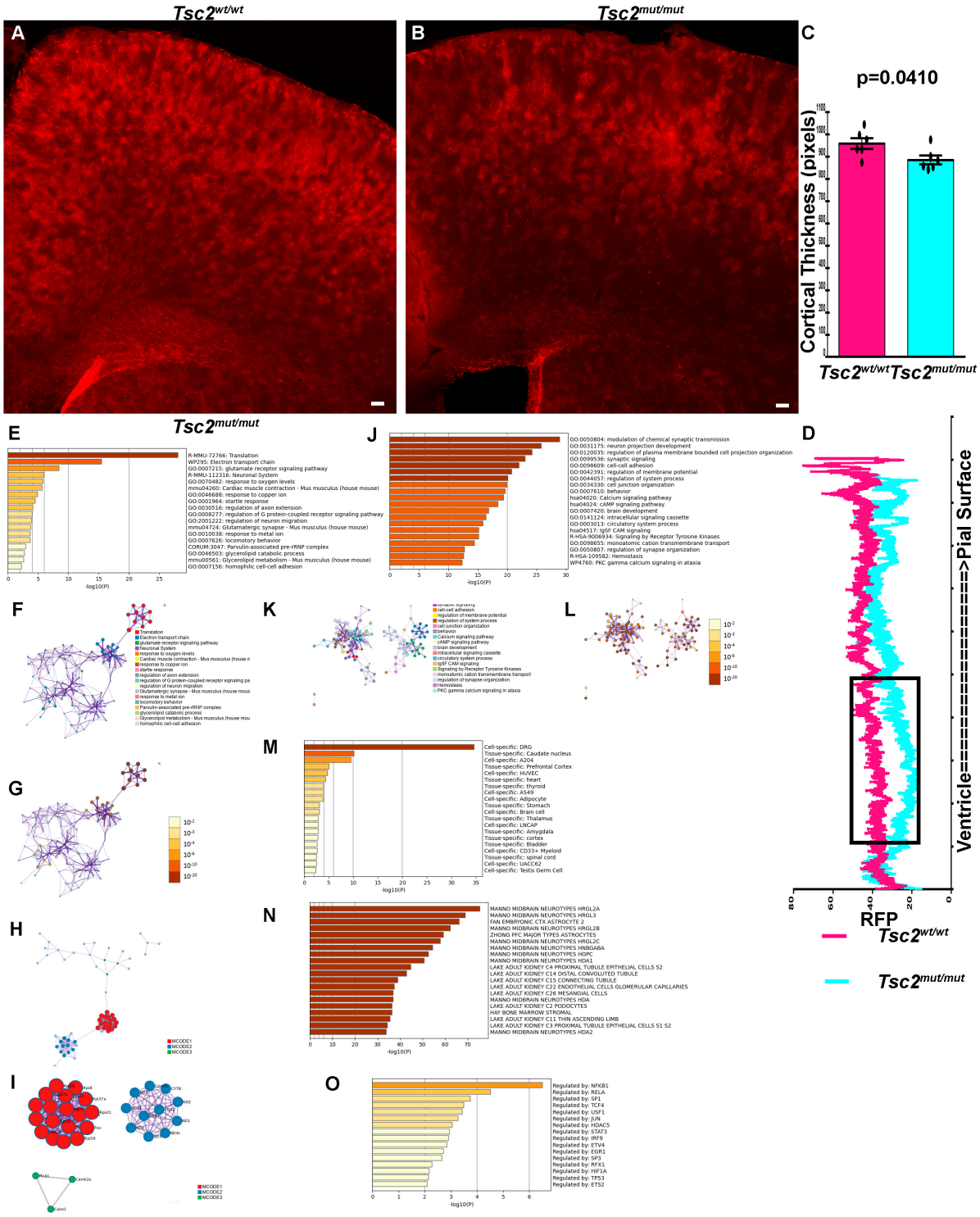



**Figure 5.** Astrocytes are Altered in TSC (**A**,**B**). 5× coronal sections of *Tsc2*$^{wt/wt}$ (**A**) or *Tsc2*$^{mut/mut}$ (**B**) mouse brains showing RFP positive cell distribution in three different mice (**C**). Quantification of cortical thickness (N = 6 for each genotype) (**D**). Quantification of RFP positive cell distribution from the ventricle to the cortical pial surface demonstrates loss of glia from lower cortical layers (N = 6 for each genotype) (**E**–**I**). Metascape Gene List Analysis of mouse *Tsc2*$^{mut/mut}$ differentially expressed transcripts in astrocytes depicting a bar graph of enriched terms across input gene lists based on *p*-values (**E**), Network of enriched terms colored by cluster ID (**F**) or *p*-value (**G**) where nodes that share the same cluster ID are typically close to each other, protein–protein interaction network and MCODE components identified in gene lists showing top three terms (**H**) and enlarged with identities (**I**). (**J**–**O**). Metascape Gene List Analysis of TSC SEGA differentially expressed transcripts in astrocytes depicting a bar graph of enriched terms across input gene lists based on *p*-values (**J**), Network

https://doi.org/10.3390/kinasesphosphatases4010006

of enriched terms colored by cluster ID (**K**) or *p*-value (**L**) where nodes that share the same cluster ID are typically close to each other, summary of enrichment analysis in PaGenBase (**M**), summary of enrichment analysis in cell type signatures (**N**), and summary of enrichment analysis in transcription factor targets (**O**). Scale bar = 50 μm.

## 3. Discussion

Here, we report neuropathological phenotypes associated with *Nestin*-CRE-ER$^{T2}$ × RFP × *Tsc2* mice. We confirmed labeling of the progeny and stem cells of the V-SVZ and hippocampus. We confirmed labeling of neuroblasts migrating to the olfactory bulb or astrocytes in the striatum and cortex that are produced from these stem cells [25]. p4EBP was detected in V-SVZ cells, including NSCs, but p4EBP was absent in wild-type astrocytes. We cannot rule out that p4EBP is below the threshold of detection for astrocytes in this study. We found that removal of *Tsc2* increased p4EBP, as we previously demonstrated in focal knockout using neonatal electroporation of CRE in the same conditional *Tsc2* mice. Cells outside of the V-SVZ continued to have elevated p4EBP following loss of *Tsc2*. In most slices, we found 2–4 cytomegalic cells having a neuron-like morphology within the dorsal-lateral striatum that stained positive for NeuN or Sox2. Neurons were also prevalent along the ventral V-SVZ near the anterior commissure, which is consistent with *Tsc1* or focal neonatal electroporation *Tsc1* or *Tsc2* models. However, the extent to which this represents a completely "mutant" phenomenon is unclear, as neurons were also identified in control conditions. We previously placed this increase at ~3× and ~7× the number of neurons compared to ventral and lateral control conditions [21].

Neonatal electroporation of *Tsc2* mice, loss of *Tsc1* by *Nestin*-CRE-ER$^{T2}$, or *Mash1*-CRE-ER$^{T2}$, or double *Tsc1/PTEN* knockout using *Nestin*-CRE-ER$^{T2}$ generates subependymal nodules or subependymal giant cell astrocytoma-like lesions [18–21,24]. We hypothesized that *Tsc2* inactivation in neonatal NSCs would generate SENs and SEGAs. We identified cellular anomalies with high penetrance that correspond to TSC pathological features. The most frequent defects were within the striatum but were heterogeneous in appearance. They could be categorized as ectopic disorganized neuronal clusters or glia-like heterotopias. Whereas neurons were pS6 positive, cells that were glia-like were p4EBP positive. However, lesions appearing to protrude into the lateral ventricles reminiscent of SEGAs in patients were rarely seen.

Subependymal nodules are common TSC brain malformations [1,36]. They are small (<1 cm) protrusions near the interface of the subependymal/subventricular zone, lateral ventricles, and striatum and frequently appear early in life [7,37]. They look "button-like" or as "candle-gutterings" [38,39]. In addition to their anatomical appearance as "growths", they can be discolored in comparison to the surrounding tissue. TSC SENs are often found before the age of five [7]. However, the actual prevalence at young ages is likely higher and may go unnoticed since the mean age of TSC diagnosis was 7.5 years of age in 2011. Screening for SENs is uncommon, and specific neurological manifestations are not yet attributed to SENs [40]. However, having SENs (having more than 2) is also a major diagnostic criterion of TSC [41].

Approximately 1/5th of TSC patients have growths around the ventricles larger than SENs called subependymal giant cell astrocytomas (SEGAs) [7,36,42]. SEGAs have profound heterogeneity, which might be a product of a specific procession of events. It appears that SENs transform into SEGAs in some patients [43–47]. In some reports, SENs are not easily detectable by routine MRI screening and are instead found during operation, postoperatively, or posthumously [45]. Computed tomography scans better detect SENs. Thus, the immediate appearance of SEGAs in the absence of a SEN could be a limitation of diagnostic imaging and monitoring. Nevertheless, SENs and SEGAs share

histopathological features, and therefore it is reasonable to consider SENs as precursors to SEGAs [20]. Although there is no consensus, the criterion of SEGA diagnosis ranges from >0.5–1.0 cm in size or serial growth [46,47]. SEGAs typically with a greater than 10 mm diameter near the foramen of Monro are also monitored for growth by MRI coupled with gadolinium [48]. SEGAs form early in life, with the median age of SEGA diagnosis at 1 and high growth rates in children during brain development [37]. While the model presented here shares some aspects of SENs and SEGAs, they rarely protrude into the ventricle.

TSC patients also commonly have cerebrocortical malformations (~90%) called tubers [3]. Cortical tubers are regions of the cerebral cortex that are mislaminated. Tubers frequently have cytomegalic dysmorphic neurons [49]. They are the site or origin of seizures and are targeted for surgical resection in cases of TSC pharmacologically resistant epilepsy [50]. Cortical tubers can also have gliosis and immune cell infiltration. Cortical tubers are assumed to arise from embryonic NSCs that undergo loss of heterozygosity [3]. This can be modeled by performing in utero electroporation [31]. We found occasional neurons in the cerebral cortex of the *Nestin*-CRE-ER$^{T2}$ × *Tsc2*$^{f/f}$ mouse. In comparison to previous studies using *Tsc1* mice, the *Tsc2*$^{f/f}$ mouse had far fewer cortical neurons [19]. However, in *Tsc2* mutant mice, we found cortical abnormalities consistent with TSC pathology, including the presence of a mislaminated cortex having sparse NeuN labeling and round giant or balloon-like cells that were pS6 positive. Incidentally, the majority of RFP positive cells in the cortical plate were astrocytes. We found that lower layers of the cerebral cortex had fewer astrocytes. Loss of *Tsc* genes from radial glia during embryogenesis causes an increase in glia [30,51–56]. These studies have identified that there are negligible effects on radial glia proliferation as measured by thymidine analog or PCNA labeling [30]. GFAP-CRE × *Tsc2* conditional mice have no difference in Pax6-positive radial glia [30]. However, they have more Tbr2 positive cells that are produced at the expense of Tbr1 positive embryonic neurons and FoxP2 positive lower layer neurons. Moreover, a recent study has described that removal of *Tsc1/Tsc2* causes an increase in the number of intermediate progenitors, upper layer neurons, and GFAP-positive cells [33] These studies are consistent with a proposed role for mTORC1 signaling, which regulates the balance of cell division types (terminal vs. self-renewing) in the V-SVZ [22,28]. Moreover, studies have found that the removal of *Tsc1* in postnatal V-SVZ NSCs did not change the rate of proliferation of NSCs cultured in vitro [18]. It was previously demonstrated that enhanced mTORC1-dependent translation alters NSC and progenitor transitional events following loss of *Tsc2* [21]. One possibility is that loss of *Tsc2* in dorsal radial glia during the postnatal period may alter the types of cells produced or enhance the production of upper-layer astrocytes at the expense of lower-layer astrocytes. It may also be possible that the effects that occur depend on the timing of the loss of *Tsc* genes and which mRNAs are present in which cells. Future studies should distinguish between these possibilities, the importance of timing of loss of TSC genes in gliogenic stem cells, and whether the mode of division (for example, self-renewing cell division vs. terminal cell division producing neurons or glia) may be disrupted. Occasional cells that appear similar to giant cells were discovered. These cells may require several weeks or months to gain the characteristics of the pathognomonic "giant cells" of TSC, as previously reported using a doxycycline *Nestin*-CRE system induced during embryogenesis [57].

Given the large number of cells affected, one question is why there are so few lesions even within a given mouse that has a lesion. It is unclear what percentage of cells lose both copies of *Tsc2* in this model. First, our studies point to the requirement to lose both copies of a TSC allele. They do not rule out the possibility that some pathogenic variants in *TSC1* or *TSC2* may only require heterozygosity for the formation of lesions. In addition, there may be single-nucleotide polymorphisms that collaborate with pathogenic heterozygous

mutations to cause gross anatomical defects in TSC. ~2.4% of SEGAs were identified after age 40 in one study, refuting the probability of mutation of genes other than *TSC1* and *TSC2* as a significant cause of SEGAs [58]. Also, fewer than 10% of patients have bilateral SEGAs, but of all patients with SEGAs, ~45% have multiple or bilateral SEGAs. This result supports the idea that predisposing factors might make some patients more susceptible to developing SEGAs. This could be related to genotype since 13.2% of all patients have SEGAs with *TSC1* mutations and 33.7% of all patients have SEGAs with *TSC2* mutations [37]. Accordingly, in that comprehensive study, ~89.3% of all patients having SEGAs had mutations identified in *TSC2*. In addition, *PKD1* is oriented in a tail-to-tail configuration with the *TSC2* gene. Mutations affecting both genes cause *PKD1-TSC2* contiguous gene syndrome, but this occurs in an estimated 3% of TSC cases and leads to polycystic kidney phenotypes and SEGAs [59]. Given that genetic testing may overlook the involvement of *PKD1*, its contribution to SEGA formation may be more common than currently recognized. Bilateral SEGAs are predicted to occur more frequently in patients with familial inherited TSC gene mutations and unilaterally in sporadic TSC. This idea aligns with Alfred Knudson's proposed two-hit theory, indicating that TSC hamartomas are caused by LOH [8,15]. Indeed, *TSC1* or *TSC2* LOH occurs in SEGAs [60–63]. Involvement of additional mutations, including in the proto-oncogene *BRAF* encoding the B-Raf kinase, have dissolved with only *TSC1* or *TSC2* mutations consistently identified [60]. Nevertheless, it remains to be seen whether additional genetic or epigenetic events contribute to the appearance and growth of SEGAs.

Bioinformatic analysis of $Tsc2^{mut/mut}$ astrocytes indicated changes in translational regulation pathways, which may be related to stalled mRNA translation. Importantly, some of the differentially expressed transcripts were also previously identified as differentially expressed in $Tsc2^{mut/mut}$ V-SVZ NSC cultures. While we also previously reported a small percentage of astrocytes in patient SEGAs from snRNA sequencing, we did not report on the bioinformatic analysis of differentially expressed transcripts. While many differentially expressed transcripts were shared between cell types, here we report the bioinformatic analysis of all of the transcripts. This analysis highlighted the conservation with transcripts found within the caudate and with cortical astrocytes and striatal radial-glia-like cells, consistent with their proposed identity.

Although there was tremendous heterogeneity in TSC mouse phenotypes, it is noteworthy that some anatomical defects were not bilaterally localized within the mice, arguing against the genetic background being the major driver of phenotypes. Moreover, despite several of the same cell types affected, the phenotypes appeared stochastically. Some TSC brain malformations have been theorized to arise from stem cells that are enriched in humans and are sparse in rodents, which could also be a reason that brain lesions are rare in this model. It is also possible that the cell types responsible for TSC phenotypes are infrequently targeted in the *Nestin*-CRE-$ER^{T2}$ model when tamoxifen is provided during the early neonatal period. While this is the most parsimonious reason that cortical malformations are rare, given that we previously indicated that tubers were caused by loss of heterozygosity within embryonic NSCs (radial glia), we would have predicted that SENs/SEGAs and striatal hamartomas should be produced [18–21,24,31,64,65]. However, they were not efficiently generated, which could be related to inefficient recombination in a cell type. Given the cellular diversity of SEGAs and the abundance of GABAergic neurons in SEGAs, it remains unclear which cells are the pathogenic driver of their formation and whether this cell type is efficiently targeted in the reported model [35].

## 4. Materials and Methods

### *4.1. Animals*

All experiments were approved and performed according to the Clemson University Institutional Animal Care and Use Committee and were compliant with the Animal Care and Use Review Office (ACURO), a component of the USAMRDC Office of Research Protections (ORP) within the Department of Defense (DoD). Mouse strains were tdTomato (B6.Cg-*Gt(ROSA)26Sor*$^{tm9(CAG\text{-}tdTomato)Hze/J}$) (Strain #007909), *Nestin*-CRE-ER$^{T2}$ (C57BL/6-Tg$^{(Nes\text{-}cre/ERT2)KEisc/J}$) (Strain #:016261), and Tsc2$^{tm1.1Mjg/J}$ (Strain #027458) and were acquired from Jackson Laboratories [26,66]. Mice were housed under standard pathogen-free conditions with a 12 h light/dark cycle and fed ad libitum. Mice were injected with 20–50 µg/g (Z)-4-Hydroxy-tamoxifen (Sigma Aldrich, Saint Louis, MO, USA, Cat#H7904) between P0-P2 for two days as previously described [21,25]. Mice were injected with 2.2 µg/g EdU (Invitrogen, Carlsbad, CA, USA, #C10337) at the time of tamoxifen treatment or, where indicated, 2 h prior to sacrifice. Alternatively, *Tsc2*$^{f/f}$ or *Tsc2*$^{wt/wt}$ × RFP mice were electroporated with CRE recombinase and GFP encoding plasmids as previously described [23].

### *4.2. Genotyping PCR*

Genotyping was performed as previously described [21]. Briefly, samples were digested in 50 mM NaOH with 0.2 mM EDTA at 50 °C for 90 min. Digestions were terminated by adding an equal volume of 100 mM Tris-HCl. Samples were briefly vortexed, centrifuged, and subjected to standard PCR reactions. Primer sequences were, 5′-ACAATGGGAGGCACATTACC-3′ and 5′AGCAGCAGGTCTGCAGTG-3′ (for *Tsc2*), 5′-AAGGGAGCTGCAGTGGAG TA-3′ and 5′-CCG AAAATCTGTGGGAAG TC-3′ and 5′-GGCATTAAAGCAGCGTATCC-3′ and 5′-CTGTTCCTGTACGGCATGG-3′ (tdTomato or wild-type amplicon), or 5′-ATGCAGGCAAATTTTGGTGT-3′ and 5′-CGCCGCTACTTCTTTTCA AC-3′ and 5′-AGTGGCCTCTTCCAGAAATG-3′ and 5′-TGCGACTGTGTCTGATTTCC-3′ (control). Additionally, mice were genotyped with 5′-ATACCGGAGATCATGCAAGC-3′ (CRE) and 5′-GGCCAGGCTGTTCTTCTTAG-3′ and 5′-CTAGGCCAAGAATTGAAAGATCT-3′ and 5′-GTAGGTGGAAATTCTAGCATCATCC-3′.

### *4.3. Immunohistochemistry*

Euthasol (50 mg/kg) was administered by intraperitoneal injection followed by decapitation. Brains were dissected at room temperature in PBS and placed overnight at 4 °C in 4% paraformaldehyde (in PBS). Brains were rinsed with PBS, mounted in agarose (3%), and sectioned on a Leica VTS 1000 vibratome. Sections were blocked with 2% BSA, 0.1% Triton X-100, 0.1% Tween-20 in PBS for 1 h at room temperature. PBS containing 0.1% Tween-20 was used to subsequently stain sections three times. Sections were subsequently incubated in primary antibody overnight at 4 °C. Primary antibodies were: anti-p4EBP (1:500; Cell Signaling Technology, Danvers, MA, USA; Thr37/46, 236B4; #2855; RRID: AB_560835), anti-pS6 (1:500; Cell Signaling Technology, Danvers, MA, USA; Ser 240/244, 61H9, #4838; RRID: AB_659977;), anti-Dcx (1:500; Santa Cruz Biotechnology, Dallas, TX, USA, sc-8066 and sc-271390; RRID: AB_2088494), anti-Sox2 (1:500; Invitrogen, Carlsbad, CA, USA, 14-9811-82; RRID: AB_11219471) anti-Nestin (1:500; Novus Biologicals, Centennial, CO, USA; #NB100-1604; RRID: AB_2282642), anti-glutamine synthetase (1:500; Sigma Aldrich, Saint Louis, MO, USA,; #G2781; RRID: AB_259853), and anti-NeuN (1:500; Sigma Aldrich, Saint Louis, MO, USA,; #MAB377; RRID: AB_2298772). Samples were washed three times in PBS containing 0.1% Tween-20. Sections were incubated with the appropriate secondary antibody (Alexa Fluor series; 1:500; Invitrogen, Carlsbad, CA, USA) overnight at 4 °C. EdU staining was assessed using the Click-IT EdU h imaging kit (Invitrogen, Carlsbad, CA, USA,

C10338) according to the manufacturer's directions. Sections were mounted in ProLong Gold or Prolong Glass Antifade Mountant (ThermoFisher, Carlsbad, CA, USA, Cat# P36930 and P36984), covered with a coverslip, and nail polish was used to seal the samples. Images were acquired on a Leica (Wetzlar, Germany) SPE spectral confocal microscope with ×63 oil immersion objective, ×20 dry objective, or ×5 dry objectives.

### *4.4. Image Analysis*

Images were uploaded and analyzed on FIJI (ImageJ 1.5 g). The freehand selection tool was used to trace a region of interest (ROI) on RFP positive and RFP negative cells in the same Z section. The mean gray value was used to quantify the p4EBP staining intensity represented as the ratio of RFP positive/RFP negative for $Tsc2^{wt/wt}$ and $Tsc2^{mut/mut}$ conditions. Striatal glia p4EBP or Sox2 was quantified for individual RFP positive and RFP negative cells in a given Z section for $Tsc2^{wt/wt}$ and $Tsc2^{mut/mut}$ conditions. The ventral portion of the V-SVZ from the same slice and region was traced to quantify the area of RFP positive cells from $Tsc2^{wt/wt}$ and $Tsc2^{mut/mut}$ mice. The distance from the dorsal aspect of the lateral ventricle to the pia surface was measured using the line tool. The distribution of glia within the dorsal forebrain was measured by drawing a line from the dorsal lateral ventricle to the pia surface. The histogram values of RFP positive cells starting from the ventricle to the outer cortical region were then exported into GraphPad and represented as the RFP signal in relation to distance. Penetrance was quantified by determining the presence of heterotopic clusters of cells. 5× or 10× images of coronal brain sections were taken by personnel blinded to readouts. Images were taken by two different scientists at the time points analyzed (for P30 and P60). Other scientists documented and assessed the cellular organization and noted the presence of heterotopias. Penetrance was defined as the presence of one heterotopia in a brain.

### *4.5. Bioinformatic Analysis*

Differentially expressed transcripts derived from *Tsc2* conditional mice or patients were previously reported [21,35]. Differentially expressed transcripts from astrocyte-identified cultures were searched using Metascape (v3.5.20260201) bioinformatic analysis [67].

### *4.6. Statistics*

Data were graphed and analyzed with GraphPad Prism software (Version 8.2.0, GraphPad Software Inc., San Diego, CA, USA). Statistical significance was determined by Student's *t*-test. Quantification was performed on 5–6 randomized mice per condition per time point unless otherwise noted. N represents the number of animals, and n represents the number of cells. Error bars are reported as the standard error mean.

**Author Contributions:** Conceptualization, J.C.H., A.M.S. and D.M.F.; Methodology, J.C.H., V.A.R., L.J.F. and A.M.S.; Validation, J.C.H., V.A.R., L.J.F. and A.M.S.; Formal analysis, D.M.F. and L.J.F.; Investigation, J.C.H., V.A.R., A.M.S. and D.M.F.; Resources, D.M.F.; Data curation, J.C.H. and D.M.F.; Writing—original draft, D.M.F.; Writing—review and editing, J.C.H., V.A.R. and D.M.F.; Visualization, J.C.H.; Supervision, J.C.H. and D.M.F.; Project administration, J.C.H. and D.M.F.; Funding acquisition, D.M.F. All authors have read and agreed to the published version of the manuscript.

**Funding:** This research was funded by the [United States Department of Defense], grant number [W81XWH2010447].

**Institutional Review Board Statement:** Clemson University Institutional Animal Care and Use Committee approved all performed experiments (AUP2019-0084-01, approved in 17 January 2020), and all guidelines set forth by the Clemson University Institutional Animal Care and Use Committee and were compliant with the Animal Care and Use Review Office (ACURO), a component of the USAMRDC Office of Research Protections (ORP) within the Department of Defense (DoD).

**Informed Consent Statement:** Not applicable.

**Data Availability Statement:** The original contributions presented in this study are included in the article. Further inquiries can be directed to the corresponding author.

**Conflicts of Interest:** DMF served as a consultant for Neurohope Therapeutics and is a member of the TSC Alliance Preclinical Consortium. VAR is a current employee at Cincinnati Children's Hospital Medical Center. AMS has worked with OrphAI Therapeutics and/or Halda Therapeutics.

## References


1. Hasbani, D.M.; Crino, P.B. Tuberous Sclerosis Complex. In *Handbook of Clinical Neurology*; Elsevier: Amsterdam, The Netherlands, 2018; Volume 148, pp. 813–822.
2. Feliciano, D.M.; Lin, T.V.; Hartman, N.W.; Bartley, C.M.; Kubera, C.; Hsieh, L.; Lafourcade, C.; O'Keefe, R.A.; Bordey, A. A Circuitry and Biochemical Basis for Tuberous Sclerosis Symptoms: From Epilepsy to Neurocognitive Deficits. *Int. J. Dev. Neurosci.* **2013**, *31*, 667–678. [CrossRef]
3. Feliciano, D.M. The Neurodevelopmental Pathogenesis of Tuberous Sclerosis Complex (TSC). *Front. Neuroanat.* **2020**, *14*, 39. [CrossRef]
4. The European Chromosome 16 Tuberous Sclerosis Consortium. Identification and Characterization of the Tuberous Sclerosis Gene on Chromosome 16. *Cell* **1993**, *75*, 1305–1315. [CrossRef]
5. Van Slegtenhorst, M.; De Hoogt, R.; Hermans, C.; Nellist, M.; Janssen, B.; Verhoef, S.; Lindhout, D.; Van Den Ouweland, A.; Halley, D.; Young, J.; et al. Identification of the Tuberous Sclerosis Gene TSC1 on Chromosome 9q34. *Science (1979)* **1997**, *277*, 805–808. [CrossRef]
6. Henske, E.P.; Jóźwiak, S.; Kingswood, J.C.; Sampson, J.R.; Thiele, E.A. Tuberous Sclerosis Complex. *Nat. Rev. Dis. Primers* **2016**, *2*, 16035. [CrossRef] [PubMed]
7. Chan, D.L.; Calder, T.; Lawson, J.A.; Mowat, D.; Kennedy, S.E. The Natural History of Subependymal Giant Cell Astrocytomas in Tuberous Sclerosis Complex: A Review. *Rev. Neurosci.* **2018**, *29*, 295–301. [CrossRef] [PubMed]
8. Knudson, A.G. Mutation and Cancer: Statistical Study of Retinoblastoma. *Proc. Natl. Acad. Sci. USA* **1971**, *68*, 820–823. [CrossRef]
9. Yeung, R.S.; Xiao, G.H.; Jin, F.; Lee, W.C.; Testa, J.R.; Knudson, A.G. Predisposition to Renal Carcinoma in the Eker Rat Is Determined by Germ- Line Mutation of the Tuberous Sclerosis 2 (TSC2) Gene. *Proc. Natl. Acad. Sci. USA* **1994**, *91*, 11413–11416. [CrossRef]
10. Hino, O.; Klein-Szanto, A.J.P.; Freed, J.J.; Testa, J.R.; Brown, D.Q.; Vilensky, M.; Yeung, R.S.; Tartof, K.D.; Knudson, A.G. Spontaneous and Radiation-Induced Renal Tumors in the Eker Rat Model of Dominantly Inherited Cancer. *Proc. Natl. Acad. Sci. USA* **1993**, *90*, 327–331. [CrossRef]
11. Xiao, G.H.; Jin, F.; Yeung, R.S. Germ-Line Tsc2 Mutation in a Dominantly Inherited Cancer Model Defines a Novel Family of Rat Intracisternal-A Particle Elements. *Oncogene* **1995**, *11*, 81–87.
12. Yeung, R.S.; Katsetos, C.D.; Klein-Szanto, A. Subependymal Astrocytic Hamartomas in the Eker Rat Model of Tuberous Sclerosis. *Am. J. Pathol.* **1997**, *151*, 1477–1486. [PubMed]
13. Wenzel, H.J.; Patel, L.S.; Robbins, C.A.; Emmi, A.; Yeung, R.S.; Schwartzkroin, P.A. Morphology of Cerebral Lesions in the Eker Rat Model of Tuberous Sclerosis. *Acta Neuropathol.* **2004**, *108*, 97–108. [CrossRef] [PubMed]
14. Kubo, Y.; Mitani, H.; Hino, O. Allelic Loss at the Predisposing Gene Locus in Spontaneous and Chemically Induced Renal Cell Carcinomas in the Eker Rat. *Cancer Res.* **1994**, *54*, 2633–2635. [PubMed]
15. Kubo, Y.; Klimek, F.; Kikuchi, Y.; Bannasch, P.; Hino, O. Early Detection of Knudson's Two-Hits in Preneoplastic Renal Cells of the Eker Rat Model by the Laser Microdissection Procedure. *Cancer Res.* **1995**, *55*, 989–990.
16. Kobayashi, T.; Urakami, S.; Hirayama, Y.; Yamamoto, T.; Nishizawa, M.; Takahara, T.; Kubo, Y.; Hino, O. Intragenic Tsc2 Somatic Mutations as Knudson's Second Hit in Spontaneous and Chemically Induced Renal Carcinomas in the Eker Rat Model. *Jpn. J. Cancer Res.* **1997**, *88*, 254–261. [CrossRef]
17. Kútna, V.; O'Leary, V.B.; Newman, E.; Hoschl, C.; Ovsepian, S.V. Revisiting Brain Tuberous Sclerosis Complex in Rat and Human: Shared Molecular and Cellular Pathology Leads to Distinct Neurophysiological and Behavioral Phenotypes. *Neurotherapeutics* **2021**, *18*, 845–858. [CrossRef]
18. Zhou, J.; Shrikhande, G.; Xu, J.; Mckay, R.M.; Burns, D.K.; Johnson, J.E.; Parada, L.F. Tsc1 Mutant Neural Stem/Progenitor Cells Exhibit Migration Deficits and Give Rise to Subependymal Lesions in the Lateral Ventricle. *Genes Dev.* **2011**, *25*, 1595–1600. [CrossRef]
19. Feliciano, D.M.; Quon, J.L.; Su, T.; Taylor, M.M.; Bordey, A. Postnatal Neurogenesis Generates Heterotopias, Olfactory Micronodules and Cortical Infiltration Following Single-Cell TSC1 Deletion. *Hum. Mol. Genet.* **2012**, *21*, 799–810. [CrossRef]
20. Zordan, P.; Cominelli, M.; Cascino, F.; Tratta, E.; Poliani, P.L.; Galli, R. Tuberous Sclerosis Complex-Associated CNS Abnormalities Depend on Hyperactivation of MTORC1 and Akt. *J. Clin. Investig.* **2018**, *128*, 1688–1706. [CrossRef]

21. Riley, V.A.; Shankar, V.; Holmberg, J.C.; Sokolov, A.M.; Neckles, V.N.; Williams, K.; Lyman, R.; Mackay, T.F.C.; Feliciano, D.M. Tsc2 Coordinates Neuroprogenitor Differentiation. *iScience* **2023**, *26*, 108442. [CrossRef]
22. Feliciano, D.M.; Bordey, A. TSC-MTORC1 Pathway in Postnatal V-SVZ Neurodevelopment. *Biomolecules* **2025**, *15*, 573. [CrossRef]
23. Holmberg, J.; Riley, V.; Sokolov, A.; Mukherjee, S.; Feliciano, D. Protocol for Electroporating and Isolating Murine (Sub-) Ventricular Zone Cells for Single Nuclei Omics. *STAR Protoc.* **2024**, *5*, 103095. [CrossRef]
24. Mukherjee, S.; Wolan, M.J.; Scott, M.K.; Riley, V.A.; Sokolov, A.M.; Feliciano, D.M. A Bitopic MTORC Inhibitor Reverses Phenotypes in a Tuberous Sclerosis Complex Model. *Sci. Rep.* **2025**, *15*, 20367. [CrossRef]
25. Riley, V.A.; Holmberg, J.C.; Sokolov, A.M.; Feliciano, D.M. Tsc2 Shapes Olfactory Bulb Granule Cell Molecular and Morphological Characteristics. *Front. Mol. Neurosci.* **2022**, *15*, 19. [CrossRef]
26. Lagace, D.C.; Whitman, M.C.; Noonan, M.A.; Ables, J.L.; DeCarolis, N.A.; Arguello, A.A.; Donovan, M.H.; Fischer, S.J.; Farnbauch, L.A.; Beech, R.D.; et al. Dynamic Contribution of Nestin-Expressing Stem Cells to Adult Neurogenesis. *J. Neurosci.* **2007**, *27*, 12623–12629. [CrossRef] [PubMed]
27. Paliouras, G.N.; Hamilton, L.K.; Aumont, A.; Joppé, S.E.; Barnabé-Heider, F.; Fernandes, K.J.L. Mammalian Target of Rapamycin Signaling Is a Key Regulator of the Transit-Amplifying Progenitor Pool in the Adult and Aging Forebrain. *J. Neurosci.* **2012**, *32*, 15012–15026. [CrossRef]
28. Hartman, N.W.; Lin, T.V.; Zhang, L.; Paquelet, G.E.; Feliciano, D.M.; Bordey, A. MTORC1 Targets the Translational Repressor 4E-BP2, but Not S6 Kinase 1/2, to Regulate Neural Stem Cell Self-Renewal In Vivo. *Cell Rep.* **2013**, *5*, 433–444. [CrossRef] [PubMed]
29. Baser, A.; Skabkin, M.; Kleber, S.; Dang, Y.; Gülcüler Balta, G.S.; Kalamakis, G.; Göpferich, M.; Ibañez, D.C.; Schefzik, R.; Lopez, A.S.; et al. Onset of Differentiation Is Post-Transcriptionally Controlled in Adult Neural Stem Cells. *Nature* **2019**, *566*, 100–104. [CrossRef] [PubMed]
30. Way, S.W.; Mckenna, J.; Mietzsch, U.; Reith, R.M.; Wu, H.C.J.; Gambello, M.J. Loss of Tsc2 in Radial Glia Models the Brain Pathology of Tuberous Sclerosis Complex in the Mouse. *Hum. Mol. Genet.* **2009**, *18*, 1252–1265. [CrossRef] [PubMed]
31. Feliciano, D.M.; Su, T.; Lopez, J.; Platel, J.C.; Bordey, A. Single-Cell Tsc1 Knockout during Corticogenesis Generates Tuber-like Lesions and Reduces Seizure Threshold in Mice. *J. Clin. Investig.* **2011**, *121*, 1596–1607. [CrossRef]
32. Magri, L.; Cambiaghi, M.; Cominelli, M.; Alfaro-Cervello, C.; Cursi, M.; Pala, M.; Bulfone, A.; Garca-Verdugo, J.M.; Leocani, L.; Minicucci, F.; et al. Sustained Activation of MTOR Pathway in Embryonic Neural Stem Cells Leads to Development of Tuberous Sclerosis Complex-Associated Lesions. *Cell Stem Cell* **2011**, *9*, 447–462. [CrossRef]
33. Casingal, C.R.; Nakagawa, N.; Yabuno-Nakagawa, K.; Meyer, C.; Liu, S.; Gkini, V.; Cho, S.-J.; Skarica, M.; Liang, D.; Simon, J.M.; et al. TSC Tunes Progenitor Balance and Upper-Layer Neuron Generation in Neocortex. *Nature* **2026**, *650*, 417–427. [CrossRef]
34. Kassai, H.; Sugaya, Y.; Noda, S.; Nakao, K.; Maeda, T.; Kano, M.; Aiba, A. Selective Activation of MTORC1 Signaling Recapitulates Microcephaly, Tuberous Sclerosis, and Neurodegenerative Diseases. *Cell Rep.* **2014**, *7*, 1626–1639. [CrossRef]
35. Holmberg, J.C.; Shankar, V.; Lyman, R.A.; Mackay, T.F.C.; Feliciano, D.M. Single Nuclei Transcriptomics Reveals Cellular Diversity in TSC Subependymal Giant Cell Astrocytomas. *iScience* **2025**, *28*, 113389. [CrossRef]
36. Northrup, H.; Krueger, D.A.; Roberds, S.; Smith, K.; Sampson, J.; Korf, B.; Kwiatkowski, D.J.; Mowat, D.; Nellist, M.; Povey, S.; et al. Tuberous Sclerosis Complex Diagnostic Criteria Update: Recommendations of the 2012 International Tuberous Sclerosis Complex Consensus Conference. *Pediatr. Neurol.* **2013**, *49*, 243–254. [CrossRef] [PubMed]
37. Jansen, A.C.; Belousova, E.; Benedik, M.P.; Carter, T.; Cottin, V.; Curatolo, P.; Dahlin, M.; D'Amato, L.; D'Augères, G.B.; De Vries, P.J.; et al. Clinical Characteristics of Subependymal Giant Cell Astrocytoma in Tuberous Sclerosis Complex. *Front. Neurol.* **2019**, *10*, 705. [CrossRef] [PubMed]
38. Crithchley, M.; Earl, C.J.C. Tuberose Sclerosis and Allied Conditions. *Brain* **1932**, *55*, 311–346. [CrossRef]
39. Lind, W.A.T. EPILOIA. *Med. J. Aust.* **1924**, *293*, 290–294. [CrossRef]
40. Staley, B.A.; Vail, E.A.; Thiele, E.A. Tuberous Sclerosis Complex: Diagnostic Challenges, Presenting Symptoms, and Commonly Missed Signs. *Pediatrics* **2011**, *127*, e117–e125. [CrossRef] [PubMed]
41. Krueger, D.A.; Northrup, H.; Krueger, D.A.; Roberds, S.; Smith, K.; Sampson, J.; Korf, B.; Kwiatkowski, D.J.; Mowat, D.; Nellist, M.; et al. Tuberous Sclerosis Complex Surveillance and Management: Recommendations of the 2012 International Tuberous Sclerosis Complex Consensus Conference. *Pediatr. Neurol.* **2013**, *49*, 255–265. [CrossRef]
42. Adriaensen, M.E.A.P.M.; Schaefer-Prokop, C.M.; Stijnen, T.; Duyndam, D.A.C.; Zonnenberg, B.A.; Prokop, M. Prevalence of Subependymal Giant Cell Tumors in Patients with Tuberous Sclerosis and a Review of the Literature. *Eur. J. Neurol.* **2009**, *16*, 691–696. [CrossRef] [PubMed]
43. Fujiwara, S.; Takaki, T.; Hikita, T.; Nishio, S. Subependymal Giant-Cell Astrocytoma Associated with Tuberous Sclerosis-Do Subependymal Nodules Grow? *Child's Nerv. Syst.* **1989**, *5*, 43–44. [CrossRef] [PubMed]
44. Morimoto, K.; Mogami, H. Sequential CT Study of Subependymal Giant-Cell Astrocytoma Associated with Tuberous Sclerosis. Case Report. *J. Neurosurg.* **1986**, *65*, 874–877. [CrossRef]

45. Cuccia, V.; Zuccaro, G.; Sosa, F.; Monges, J.; Lubienieky, F.; Taratuto, A.L. Subependymal Giant Cell Astrocytoma in Children with Tuberous Sclerosis. *Child's Nerv. Syst.* **2003**, *19*, 232–243. [CrossRef]
46. Jóźwiak, S.; Nabbout, R.; Curatolo, P. Management of Subependymal Giant Cell Astrocytoma (SEGA) Associated with Tuberous Sclerosis Complex (TSC): Clinical Recommendations. *Eur. J. Paediatr. Neurol.* **2013**, *17*, 348–352. [CrossRef] [PubMed]
47. Roth, J.; Roach, E.S.; Bartels, U.; Jóźwiak, S.; Koenig, M.K.; Weiner, H.L.; Franz, D.N.; Wang, H.Z. Subependymal Giant Cell Astrocytoma: Diagnosis, Screening, and Treatment. Recommendations from the International Tuberous Sclerosis Complex Consensus Conference 2012. *Pediatr. Neurol.* **2013**, *49*, 439–444. [CrossRef]
48. Northrup, H.; Aronow, M.E.; Bebin, E.M.; Bissler, J.; Darling, T.N.; de Vries, P.J.; Frost, M.D.; Fuchs, Z.; Gosnell, E.S.; Gupta, N.; et al. Updated International Tuberous Sclerosis Complex Diagnostic Criteria and Surveillance and Management Recommendations. *Pediatr. Neurol.* **2021**, *123*, 50–66. [CrossRef]
49. Mühlebner, A.; Van Scheppingen, J.; Hulshof, H.M.; Scholl, T.; Iyer, A.M.; Anink, J.J.; Nellist, M.D.; Jansen, F.E.; Spliet, W.G.M.; Krsek, P.; et al. Novel Histopathological Patterns in Cortical Tubers of Epilepsy Surgery Patients with Tuberous Sclerosis Complex. *PLoS ONE* **2016**, *11*, e0157396. [CrossRef]
50. Feliciano, D.M. Modeling Genetic Mosaicism of the Mammalian Target of Rapamycin Pathway in the Cerebral Cortex. *Front. Mammal Sci.* **2023**, *2*, 1231778. [CrossRef]
51. Uhlmann, E.J.; Wong, M.; Baldwin, R.L.; Bajenaru, M.L.; Onda, H.; Kwiatkowski, D.J.; Yamada, K.; Gutmann, D.H. Astrocyte-Specific TSC1 Conditional Knockout Mice Exhibit Abnormal Neuronal Organization and Seizures. *Ann. Neurol.* **2002**, *52*, 285–296. [CrossRef]
52. Jansen, L.A.; Uhlmann, E.J.; Crino, P.B.; Gutmann, D.H.; Wong, M. Epileptogenesis and Reduced Inward Rectifier Potassium Current in Tuberous Sclerosis Complex-1-Deficient Astrocytes. *Epilepsia* **2005**, *46*, 1871–1880. [CrossRef]
53. Zeng, L.H.; Bero, A.W.; Zhang, B.; Holtzman, D.M.; Wong, M. Modulation of Astrocyte Glutamate Transporters Decreases Seizures in a Mouse Model of Tuberous Sclerosis Complex. *Neurobiol. Dis.* **2010**, *37*, 764–771. [CrossRef]
54. Zeng, L.H.; Rensing, N.R.; Zhang, B.; Gutmann, D.H.; Gambello, M.J.; Wong, M. Tsc2 Gene Inactivation Causes a More Severe Epilepsy Phenotype than Tsc1 Inactivation in a Mouse Model of Tuberous Sclerosis Complex. *Hum. Mol. Genet.* **2011**, *20*, 445–454. [CrossRef] [PubMed]
55. Mietzsch, U.; McKenna, J.; Reith, R.M.; Way, S.W.; Gambello, M.J. Comparative Analysis of Tsc1 and Tsc2 Single and Double Radial Glial Cell Mutants. *J. Comp. Neurol.* **2013**, *521*, 3817–3831. [CrossRef] [PubMed]
56. Short, B.; Kozek, L.; Harmsen, H.; Zhang, B.; Wong, M.; Ess, K.C.; Fu, C.; Naftel, R.; Pearson, M.M.; Carson, R.P. Cerebral Aquaporin-4 Expression Is Independent of Seizures in Tuberous Sclerosis Complex. *Neurobiol. Dis.* **2019**, *129*, 93–101. [CrossRef] [PubMed]
57. Goto, J.; Talos, D.M.; Klein, P.; Qin, W.; Chekaluk, Y.I.; Anderl, S.; Malinowska, I.A.; Di Nardo, A.; Bronson, R.T.; Chan, J.A.; et al. Regulable Neural Progenitor-Specific Tsc1 Loss Yields Giant Cells with Organellar Dysfunction in a Model of Tuberous Sclerosis Complex. *Proc. Natl. Acad. Sci. USA* **2011**, *108*, E1070–E1079. [CrossRef]
58. Jansen, A.C.; Belousova, E.; Benedik, M.P.; Carter, T.; Cottin, V.; Curatolo, P.; D'Amato, L.; D'Augères, G.B.; De Vries, P.J.; Ferreira, J.C.; et al. Newly Diagnosed and Growing Subependymal Giant Cell Astrocytoma in Adults with Tuberous Sclerosis Complex: Results from the International TOSCA Study. *Front. Neurol.* **2019**, *10*, 821. [CrossRef]
59. Kotulska, K.; Borkowska, J.; Mandera, M.; Roszkowski, M.; Jurkiewicz, E.; Grajkowska, W.; Bilska, M.; Jóźwiak, S. Congenital Subependymal Giant Cell Astrocytomas in Patients with Tuberous Sclerosis Complex. *Child's Nerv. Syst.* **2014**, *30*, 2037–2042. [CrossRef]
60. Bongaarts, A.; Giannikou, K.; Reinten, R.J.; Anink, J.J.; Mills, J.D.; Jansen, F.E.; Spliet, W.G.M.; den Dunnen, W.F.A.; Coras, R.; Blümcke, I.; et al. Subependymal Giant Cell Astrocytomas in Tuberous Sclerosis Complex Have Consistent TSC1/TSC2 Biallelic Inactivation, and No BRAF Mutations. *Oncotarget* **2017**, *8*, 95516–95529. [CrossRef]
61. Chan, J.A.; Zhang, H.; Roberts, P.S.; Jozwiak, S.; Wieslawa, G.; Lewin-Kowalik, J.; Kotulska, K.; Kwiatkowski, D.J. Pathogenesis of Tuberous Sclerosis Subependymal Giant Cell Astrocytomas: Biallelic Inactivation of TSC1 or TSC2 Leads to MTOR Activation. *J. Neuropathol. Exp. Neurol.* **2004**, *63*, 1236–1242. [CrossRef]
62. Giannikou, K.; Zhu, Z.; Kim, J.; Winden, K.D.; Tyburczy, M.E.; Marron, D.; Parker, J.S.; Hebert, Z.; Bongaarts, A.; Taing, L.; et al. Subependymal Giant Cell Astrocytomas Are Characterized by MTORC1 Hyperactivation, a Very Low Somatic Mutation Rate, and a Unique Gene Expression Profile. *Mod. Pathol.* **2021**, *34*, 264–279. [CrossRef]
63. Henske, E.P.; Wessner, L.L.; Golden, J.; Scheithauer, B.W.; Vortmeyer, A.O.; Zhuang, Z.; Klein-Szanto, A.J.P.; Kwiatkowski, D.J.; Yeung, R.S. Loss of Tuberin in Both Subependymal Giant Cell Astrocytomas and Angiomyolipomas Supports a Two-Hit Model for the Pathogenesis of Tuberous Sclerosis Tumors. *Am. J. Pathol.* **1997**, *151*, 1639–1647.
64. Feliciano, D.M.; Zhang, S.; Quon, J.L.; Bordey, A. Hypoxia-Inducible Factor 1a Is a Tsc1-Regulated Survival Factor in Newborn Neurons in Tuberous Sclerosis Complex. *Hum. Mol. Genet.* **2013**, *22*, 1725–1734. [CrossRef]

65. Rushing, G.V.; Brockman, A.A.; Bollig, M.K.; Leelatian, N.; Mobley, B.C.; Irish, J.M.; Ess, K.C.; Fu, C.; Ihrie, R.A. Location-Dependent Maintenance of Intrinsic Susceptibility to MTORC1-Driven Tumorigenesis. *Life Sci. Alliance* **2019**, *2*, e201800218. [CrossRef] [PubMed]
66. Hernandez, O.; Way, S.; McKenna, J.; Gambello, M.J. Generation of a Conditional Disruption of the Tsc2 Gene. *Genesis* **2007**, *45*, 101–106. [CrossRef] [PubMed]
67. Zhou, Y.; Zhou, B.; Pache, L.; Chang, M.; Khodabakhshi, A.H.; Tanaseichuk, O.; Benner, C.; Chanda, S.K. Metascape Provides a Biologist-Oriented Resource for the Analysis of Systems-Level Datasets. *Nat. Commun.* **2019**, *10*, 1523. [CrossRef] [PubMed]

**Disclaimer/Publisher's Note:** The statements, opinions and data contained in all publications are solely those of the individual author(s) and contributor(s) and not of MDPI and/or the editor(s). MDPI and/or the editor(s) disclaim responsibility for any injury to people or property resulting from any ideas, methods, instructions or products referred to in the content.